Software-to-Software Comparison of End-Anchored Floating Bridge Global Analysis

Thomas Viuff[1,*], Xu Xiang[2], Bernt Johan Leira[1], and Ole Øiseth[3]

[1]Department of Marine Technology, Norwegian University of Science and Technology, N-7491 Trondheim, Norway

[2]Norwegian Public Roads Administration, N-0667 Oslo, Norway

[3]Department of Structural Engineering, Norwegian University of Science and Technology, N-7491 Trondheim, Norway

[*]Corresponding author. Email address: thomas.h.viuff@ntnu.no

ABSTRACT

Several computer programs exist to handle general multi-purpose offshore structural analysis of slender structures subjected to wave loading, although, they have not been developed with the specific purpose of floating bridge global analysis in mind. Due to the inherent complexity of a floating bridge structure, this poses a valid concern regarding the accuracy in the calculated response. Normally, the intended computer program is validated against experiments but in the case of extremely long floating bridges the size limitations of existing ocean basins necessitates the use of hybrid testing where the computer program is a part of the method to obtain the true value from the experiments. It is, therefore, crucial to get an overview of how sensitive the numerical results are to inaccurate user inputs, approximations introduced in the theory and the software implementation of the theory as well as possible settings that the user does not have access to. An extensive comparison between two commonly used commercial computer programs in the offshore industry is presented in the present paper for a global analysis of a floating pontoon bridge concept. The comparison includes modal properties as well as deterministic and stochastic structural response

due to wave loads based on coupled hydro-elastic time domain simulations. First and second order wave loads are included in the comparison as well as viscous drag. The study indicates a reasonable agreement in the response acquired by the two computer programs and highlights consequences of differences in some of the input parameters.

INTRODUCTION

The common practice when designing offshore structures is to validate the numerical analysis with experiments obtained from tests carried out in e.g. an ocean basin facility. In some cases, however, the full-scale dimensions of the structure are of such proportions that it conflicts with the size limitations of the relevant test facilities and requirements in accuracy regarding the model scale. Due to the scale of the model, a so-called hybrid test, see e.g. Stansberg et al. (2002), is usually carried out where only parts of the model are tested in the ocean basin and used for calibration of the relevant computer program. In turn, the validated computer program is used to predict the full-scale response of the entire structure. This highlights the necessity of software-to-software comparison since the software is a part of the tests to obtain the true value. For the engineers who will plan such tests, the software-to-software comparison is of uttermost importance for their informed choice and quality control purposes as well as to have an estimate on the uncertainties related to the numerical results.

In Norway the Norwegian Public Roads Administration (NPRA) is working on establishing fixed links across the many deep and wide fjords along the E39 Coastal Highway Route. The extreme depths of up to 1,300 m and widths of up to 6,000 m makes the project particularly challenging. One of the proposed structural concepts to cross the fjords is an end-anchored floating pontoon bridge described in the present paper. Due to the extreme length requirements of the bridge the validation of the numerical models fall under the hybrid test procedure mentioned above. Experimental results exist for a shorter but similar floating bridge structure from when the first floating bridges were constructed in Norway in the early 1990s and have been used as a first step in the validation of existing computer programs, see Løken and Oftedal (1990) and Xiang and Løken (2019). However, the effect of the increased slenderness of the proposed floating bridge structure is not well understood and renders the validation towards the previous experiments insufficient. Furthermore, with several numerical studies conducted in the last five years with respect to end-anchored floating pontoon bridges related to the E39 Coastal Highway Route Project, see e.g. (Xiang et al. 2017; Fu et al. 2017; Cheng et al. 2018a; Cheng et al. 2018b; Cheng et al. 2018c), either in the coupled SIMO (SINTEF Ocean 2017b) and RIFLEX (SINTEF Ocean 2017a) program, further on referred to as SIMO-RIFLEX, or OrcaFlex (Orcina 2018) focusing on the stochastic response from wind and waves, there is a significant interest in how well results obtained by the two different computer programs compare.

The use of software-to-software comparison is a necessary option when experimental data is scarce due to the high financial costs, see e.g. Karimirad et al. (2011), Sørum et al. (2017) or Robertson et al. (2014) on validation of numerical software applied to offshore floating wind turbines. Robertson et al. (2014) did an extensive comparison of several well-known computer programs within ocean engineering, including SIMO-RIFLEX. Less available literature describes comparison of computer programs with regard to long floating bridges. Statens Vegvesen (2016) described the general design of a floating bridge structure including a comparison of the dynamic wind response between OrcaFlex and an in-house software. The present paper is a continuation of a previous paper (Viuff et al. 2018) with preliminary findings on the software-to-software comparison for the global analysis of a similar end-anchored floating pontoon bridge concept. In the present paper the comparison is more rigorously carried out and with more attention to modelling details. In our experience, different software and different users can provide results with large discrepancies, which is important when assessing the reliability of large and innovative bridge concepts. The differences will diminish with the development of special software, where all approximations and settings unavailable to the user are implemented while keeping these special structures in mind. We have made our best effort to compensate for the differences in the implementation of the theory in the two computer programs, but there are still significant differences, which illustrates the challenges that need to be solved when designing new and innovative floating bridges. Focusing on a software-to-software comparison of the two computer programs, the aim of the paper is two-fold:

1) Contribute to the knowledge of the uncertainty associated with the calculated response obtained by application of commercial software for analysis of end-anchored floating pontoon bridges. 2) Highlight the structural complexity of the end-anchored floating pontoon bridge concept and the inherent sensitivity to certain input parameters related to the numerical modelling. The comparison is performed using OrcaFlex (Orcina 2018) version 10.2c and SIMO-RIFLEX (SINTEF Ocean 2017b; SINTEF Ocean 2017a) version 4.10.0.

THE BJØRNAFJORD FLOATING BRIDGE CONCEPT

The end-anchored floating pontoon bridge illustrated in Fig. 1 is one of the main concepts evaluated by NRPA for crossing the Bjørnafjord in western Norway. The floating bridge consists of a single 230 m high tower in the southern end connected to the bridge girder with 4x20 pre-tensioned stay-cables. North of the tower the bridge girder is resting on columns connected to 19 floating pontoons. The bridge has a radius of curvature in the horizontal plane of 5,000 m, resulting in a total road line of 4,602 m going from south to north. The geometry and structural properties of the bridge is based on (Statens Vegvesen 2016) and only the most relevant information is given in this section. The bridge girder consists of a twin-box cross-section modelled as a single equivalent beam with properties listed in Tab. 1. The road line at the high bridge part from AX1 to AX3 is divided into five consecutive segments of 220, 100, 100, 100, 330 and 10 m with cross-section H1, H2, H3, H2, H1 and S1, respectively. Similarly at the low bridge part from AX3 to AX22, the 197 m road line between each pontoon and between the last pontoon and the northern end is divided into three consecutive sections of 25, 147 and 25 m with cross-section S1, F1 and S1, respectively. The distribution of the cross-sections along the bridge girder is illustrated in Fig. 1.

The vertical position of the bridge girder is mainly 15 m along the low bridge part but at the tower the freeboard is roughly increased to 55 m to allow for ship traffic. Along the bridge at each pontoon, two columns are positioned perpendicular to the bridge axis consisting of circular cross-sections of varying height.

The same pontoon geometry is used for all 19 pontoons. The geometry is made up of a rectangular box in the middle, two half circle cylinders at each end and an extended bottom plate, which in the following will be referred to as a heave plate following the terminology from the offshore wind turbine industry. The pontoons are 14.5 m high, 28 m wide and 68 m long, and the heave plate is 5 m wide and 0.6 m high. All pontoons are oriented with surge along the global x-axis and sway following the global y-axis. Figure 2 illustrates the coordinate definitions and the wave directions used in the model and Tab. 2 lists the properties of the pontoon without ballast. Ballast between roughly 750 and 2,500 ton is added to the different pontoons in order to keep them all at the same draft of 10.5 m. The application of a heave plate on the pontoons is not a new concept but has been applied for many years in the offshore industry where it has been used to change the mass and damping properties of structures such as floating wind turbines (Tao and Cai 2004) or floating production storage and offloading (FPSO) units (Shao et al. 2016). The heave plate has been proposed for this bridge concept and Xiang et al. (2017) has shown that a significant reduction in the global response can be obtained from this change in the pontoon geometry.

METHODOLOGY

The numerical models created in both computer programs are based on many of the same assumptions and the same theoretical background. The present paper describes the general procedure for both computer programs and seek to point out any existing differences between them.

Numerical Model of the Floating Bridge

The structure is modelled using beam and bar elements in both computer programs and the pontoons are modelled as 6 degree of freedom (DOF) rigid bodies with mass, stiffness and damping matrices according to the relevant hydrodynamic properties. The structural damping in both computer programs is modelled using Rayleigh damping and linear material properties are applied. Rigid body connections are used to model the connections between the tower and the stay-cables, the girder and the stay-cables, the columns and the girder, and the pontoons and the columns. Both models are fixed at the bottom of the tower and at each end of the bridge, as well as in the global y-direction for the girder at AX2. The element length varies according to the location. The length of the elements are roughly 3 m for the tower, 20 m for the stay-cables, 7 to 27 m for the columns, and 10 to 20 m for the girder.

In both computer programs the hybrid frequency- and time domain method is used to solve the equation of motion, resulting in the well-known Cummins Equation (Cummins 1962).

$$q_j^{exc}(t) = \sum_{k=1}^{6} \left[M_{jk} + A_{jk}^{\infty} \right] \ddot{u}_k(t) + D_{jk}\dot{u}_k(t) + \left[K_{jk} + C_{jk} \right] u_k(t) + \int_0^{t_{mem}} k_{jk}(t-\tau)\dot{u}_k(\tau)d\tau \quad (1)$$

Here, $q_j^{exc}(t)$ represents the wave excitation load, which includes the first order wave load $q_j^{(1)}(t)$, the second order wave loads $q_j^{(2)}(t)$ and the drag load $q_j^{(d)}(t)$. The notations M_{jk}, K_{jk}, D_{jk} represent the structural mass, stiffness and damping in the system. The frequency-dependent added mass $A_{jk}(\omega)$ and damping $B_{jk}(\omega)$ are included by the added mass at infinite frequency A_{jk}^{∞} and the retardation function $k_{jk}(t)$. The time dependent displacement response and its time derivatives are symbolized by $u_k(t)$, $\dot{u}_k(t)$ and $\ddot{u}_k(t)$. Finally the time shift is denoted by τ and the time "memory" by t_{mem}.

Modelling Hydrodynamic Loads

Generating Wave Elevation

The wave elevation in the floating bridge models is based on a 3-parameter JONSWAP (Hasselmann et al. 1973) wave spectrum, see Eqn. (2), with parameters according to the 100-year wave environment at the Bjørnafjorden site (Statens Vegvesen 2017):

$$S_\zeta(\omega) = \frac{\alpha g^2}{\omega^5} \exp\left[-\frac{5}{4} \left(\frac{\omega_p}{\omega} \right)^4 \right] \gamma^{\,b} \quad (2)$$

where,

$$
\alpha = \left(\frac{H_s \omega_p^2}{4g}\right)^2 \frac{1}{0.065\gamma^{0.803} + 0.135}
$$

$$
b = \exp\left[-\frac{1}{2\sigma^2}\left(\frac{\omega}{\omega_p} - 1\right)^2\right]
$$

$$
\sigma = \begin{cases} 0.07 & \text{for} \quad \omega < \omega_p \\ 0.09 & \text{for} \quad \omega > \omega_p \end{cases}
$$

and g is the gravitational constant. The directional spreading is governed by the spreading function $D(\theta)$ where θ_0 is the main wave direction, $\Gamma(\cdot)$ is the Gamma function and s is the spreading exponent. The spreading exponent value used in the comparison is set to 4, within naturally occurring short-crested wave environments.

$$
D(\theta) = \frac{1}{\sqrt{\pi}} \frac{\Gamma(\frac{s}{2} + 1)}{\Gamma(\frac{s}{2} + \frac{1}{2})} \cos^s(\theta - \theta_0), \quad |\theta - \theta_0| \le \frac{\pi}{2} \tag{3}
$$

An important note should be made about the implementation of the directional spreading function in the two computer programs, which has a significant influence on the response characteristics in short-crested seas. The numerical implementation is based on a chosen number of wave directions, which in this study is set to 11. Based on the number of wave directions the exact wave directions are calculated automatically in both computer programs. In SIMO-RIFLEX the wave directions are chosen based on a linear distribution from $-\frac{\pi}{2}$ to $\frac{\pi}{2}$, whereas OrcaFlex distributes the wave directions according to the equal energy strategy (Orcina 2018) giving a more narrow spreading around the main wave direction. Due to the orientation and geometry of the floating pontoons even small waves in surge are expected to have a significant effect on the bridge response. In order to compensate for this difference in the two computer programs, a user specified directional wave spectrum is used in SIMO-RIFLEX based on the spectrum values and directional spreading values used in OrcaFlex.

Modelling the Pontoon-Wave Interaction

The interaction between the pontoons and the water is based on linear potential theory using Wadam (DNV 2014) for a single pontoon with the dimensions previously described. The draft is set to 10.5 meter and a double-symmetric panel model is used in the analysis. The wave directions applied goes from 0° to 90° with a resolution of 5° and the 60 wave frequencies are within 0.033 to 1 Hz with varying step length in order to give a smooth description of the first order wave load transfer function and the mean drift load. An element mesh density of 0.4 meter is applied to the panel model resulting in roughly 9,200 elements. The high resolution of the panel model is used in order to minimize the sensitivity to the mesh. Figure 3 shows the convergence of the frequency-dependent added mass in roll with respect to the panel element size as well as the convergence of the mean wave load with respect to the panel element size using both direct pressure integration (near-field method) and conservation of momentum (far-field method). The far-field method converges very fast and for the chosen mesh resolutions the result is the same. Instead the near field method shows slow or non-existing convergence for the horizontal mean drift loads. Pan et al. (2013) investigated the convergence of a panel model in Wadam with regard to the far-field and near-field solutions of mean drift loads. They tested different panel mesh quality of an LNG model, showing that for horizontal mean drift loads (surge, sway and yaw) the near-field method exhibits great difficulty to converge even for a very fine panel model, while vertical mean drift loads (heave, roll and pitch) tends to converge faster for the near-field method. Their recommendation for a common calculation is to apply the far-field method for the horizontal loads, and near-field method for the vertical loads if necessary. For the current study only horizontal mean drift loads estimated using the far-field method is considered since the focus is on comparison of the structural response and less on modelling details. The hydrodynamic coefficients calculated in Wadam are used as input for the numerical model in both computer programs.

Ballast is included in OrcaFlex by using 6 DOF buoys with the relevant inertia properties, whereas in SIMO-RIFLEX the relevant elements in the pontoon mass matrices are updated accordingly.

Buoyancy is implemented in SIMO-RIFLEX using a constant vertical force at the center of buoyancy on each pontoon and by removing the buoyancy terms for roll and pitch in the hydrostatic stiffness matrix. In OrcaFlex the buoyancy is defined by the displaced volume and the location of the center of buoyancy.

Generating First Order Wave Loads

The first order wave loads are generated by Monte Carlo simulation using fast Fourier transformation (FFT) of the real part of the product of the first order wave transfer function and the wave elevation:

$$q_j^{(1)}(x,y,t) = \Re \sum_{m=1}^{N_\omega} \sum_{n=1}^{N_\theta} \sqrt{2S_\zeta(\omega_m)D(\theta_n)\Delta\omega_m\Delta\theta_n} \left|H_j^{(1)}(\omega_m,\theta_n)\right| \exp\left[i\left(\varepsilon_{nm} + \varphi_{H_{jnm}^{(1)}}\right)\right] \exp\left[i\left(\omega_m t - k_m x\cos(\theta_n) - k_m y \sin(\theta_n)\right)\right] \tag{4}$$

where $S_\zeta(\omega_m)$ is the unidirectional wave spectrum, $D(\theta_n)$ is the directional spreading function, k_m is the wave number, ε_{nm} is the random phase angle, $H_j^{(1)}(\omega_m,\theta_n)$ is the first order wave load transfer function and $\varphi_{H_{jnm}^{(1)}}$ the phase angle.

Generating Second Order Wave Loads

In both computer programs the second order wave loads in the horizontal plane are generated by Monte Carlo simulation using second order FFT:

$$q_j^{(2)}(x,y,t) = \Re \sum_{l=1}^{N_\omega} \sum_{m=1}^{N_\omega} \sum_{n=1}^{N_\theta} \sqrt{2S_\zeta(\omega_l)D(\theta_n)\Delta\omega_l\Delta\theta_n} \left|H_j^{(2-)}(\omega_l,\omega_m,\theta_n)\right| \sqrt{2S_\zeta(\omega_m)D(\theta_n)\Delta\omega_m\Delta\theta_n} \exp\left[i\left((\omega_l-\omega_m)t + \varepsilon_{nl} + \varepsilon_{nm} + \varphi_{H_{jnlm}^{(2-)}})\right)\right] \tag{5}$$

where $H_j^{(2-)}(\omega_l,\omega_m,\theta_n)$ denotes the quadratic transfer function (QTF) of the difference-frequency wave load, and $\varphi_{H_{jnlm}^{(2-)}}$ is the phase angle. The Newman's approximation (Faltinsen 1993) is applied to simplify the above equation by reducing the full QTF data to only diagonal terms representing component pairs with identical wave direction and wave period. The consequence of the Newman approximation is that the phase angle $\varphi_{H^{(2-)}_{jnlm}} = 0$ and

$$H_j^{(2-)}(\omega_l, \omega_m, \theta_n) = \sqrt{|H_j^{(2-)}(\omega_l, \omega_l, \theta_n) H_j^{(2-)}(\omega_m, \omega_m, \theta_n)|} \tag{6}$$

taken as the geometric mean. The Newman's approximation is most likely not valid for the short-crested sea used in the present study. However, since the focus of the paper is more on how well the two computer programs compare than on making the analysis completely physically correct, the authors find that the results obtained from the comparison would still be of interest to the reader.

The mean drift load coefficients are in principle influenced by the first order motion, which is unknown before the final hydro-elastic time-domain simulation is made. As a consequence the coefficients should be obtained based on an iterative loop between the radiation and diffraction analysis and the following time-domain simulations. As a first approximation of the mean wave load in the present study, however, the pontoon is fixed in its mean position in all six DOFs in the Wadam analysis. With a focus on comparing the two computer programs, this approximation is acceptable for the present study.

Modelling Viscous Effects

The viscous effects on the pontoons are modelled as drag loads using Morison elements. Equation (7) describes the viscous drag load for a single element in the local element coordinate system.

$$q_j^{(d)}(t) = \frac{1}{2} \rho C_j^d A_j u_r(t) \, |u_r(t)| \tag{7}$$

Where C_j^d is the quadratic drag coefficient, ρ is the density of the water, A_j is the cross-sectional area in direction j and $u_r(t)$ is the relative velocity of the water at the Morison element.

Different values have been suggested for the quadratic drag coefficients. Xiang et al. (2017) suggested a vertical drag coefficient of 4.2 according to model tests and supporting literature, whereas Cheng et al. (2018a) used a more conservative estimation of $C_x^d = 1.0$, $C_y^d = 0.6$ and $C_z^d = 2.0$ following the global coordinate system notation. The latter option is applied in the present study.

For each pontoon two Morison elements are used, and these are oriented with the axial direction pointing along the positive global z-axis The first element starts at the bottom of the pontoon and continues up to the top of the heave plate. The second element starts at the top of the heave plate and continues up to the mean water line. The cross-sectional areas in the three directions for the first element are $A_x^{(1)} = 47\ \mathrm{m}^2$, $A_y^{(1)} = 23\ \mathrm{m}^2$ and $A_z^{(1)} = 2654\ \mathrm{m}^2$. Similarly for the second element the values are $A_x^{(2)} = 673\ \mathrm{m}^2$, $A_y^{(2)} = 277\ \mathrm{m}^2$ and $A_z^{(2)} = 0\ \mathrm{m}^2$.

Modelling Structural Properties

The presented computer programs make use of the Finite Element Method (FEM) formulation to combine the structural and hydrodynamic parts into a complete Finite Element (FE) model. The theory of FEM is well-known and will not be covered here. For more detailed information the reader is referred to the respective theory manuals for the two computer programs (SINTEF Ocean 2017a; Orcina 2018). Instead a short description of the relevant assumptions is given in this section following the nomenclature within each of the two theory manuals, see Fig. 4 for a clarification of the nomenclature.

Line Theory

The lines in both computer programs are comprised of the same FE structure as illustrated in Fig. 4 and the smallest FE unit is the element/segment between each node, which model the axial and torsional properties using sets of springs and dampers. The bending properties are represented by springs and dampers at each node and mass properties are lumped to the nodes. Both computer programs are capable of including non-isotropic bending stiffness and non-linear geometric stiffness used in the comparison. Large rotations of the elements/segments are made possible by implementing Green strain theory to account for geometric stiffness. Linear material properties are defined for each element/segment cross-section and no torsion-bending coupling or torsion-tension coupling is included. Bending stiffness properties are modelled using Bernoulli-Euler beam theory.

Note on Modelling the Twin-Box Bridge Girder

The bridge girder is modelled as a single equivalent beam in both computer programs based on the properties listed in Tab. 1. In SIMO-RIFLEX the radius of gyration is given as a single value for the cross-section, whereas in OrcaFlex the radius of gyration is estimated based on user specified inertial values for each box in the twin-box cross-section. The effect of this difference is unknown but thought to be insignificant for the analysis.

Structural Damping

The structural damping is modelled as Rayleigh damping, see Eqn. (8), in both computer programs and the mass proportional damping coefficient μ and the stiffness proportional damping coefficient λ are based on a target damping ratio ξ of less than 2 % in the frequency range of the natural periods and the wave spectrum.

$$\xi = \frac{1}{2}\left(\frac{\mu}{\omega} + \lambda\omega\right) \tag{8}$$

For the target value of the damping ratio the corresponding damping coefficients used are $\mu = 0.0025$ and $\lambda = 0.02$. The damping ratio for the first two natural frequencies are thereby given as 1.22 % and 0.83 %, respectively.

Solution Procedures

Finding Static Equilibrium

The static equilibrium is found through incremental loading of the external forces and using an iterative procedure (SINTEF Ocean 2017a; Orcina 2018). In SIMO-RIFLEX this iterative procedure is the Newton-Raphson iteration procedure.

Solving the Standard Eigenvalue Problem

In both computer programs the iterative Lanczos Method is applied when solving the standard eigenvalue problem of the system. In this method the hydrodynamic added mass of the pontoons is taken into account by summing the added mass at infinite frequency and the structural mass of the pontoons before solving the equations. The main drawback of this method is that the frequency-dependent added mass is simplified into a constant value. The natural periods found based on this method are denoted by T_n, where n is the number of the mode. In order to account for the exact added mass a method based on the pseudo procedure described in Table 3 is performed manually for SIMO-RIFLEX. The method is based on the initial set of frequencies ω_n and implies an iteration at each frequency by assuming that the corresponding modeshape remains the same. By manually defining the added mass as the exact added mass at the corresponding frequency, i.e. $A_{jk}(\omega_n)$, the final solution is obtained when the difference between two consecutive frequencies is below a user specified tolerance. The natural periods found based on this method are denoted by T_n^a. In OrcaFlex the exact added mass is accounted for in the T_n^b values which are found manually using a graphical method. In the graphical method the modeshapes are again assumed to remain in the original order and shape. By first solving the standard eigenvalue problem 60 times for each of the 60 hydrodynamic added mass values a line can be drawn for each mode in a coordinate system with two axes representing periods. This line contains the horizontal coordinate values equal to the 60 periods related to the hydrodynamic added mass values inserted in the standard eiganvalue problem. The vertical coordinate values represent natural periods of the relevant mode for each solution to the standard eigenvalue problem. By drawing a second line with the same horizontal and vertical period values representing the equation $T_j = T_j$ the solution is found as the intersection between these two lines.

Solving the Time-Domain Equations

Equation (1) is a non-linear time domain equation which includes geometric stiffness and hydrodynamic loading. The solution is found in SIMO-RIFLEX using a step-by-step numerical integration based on the Newmark β-family integration method (SINTEF Ocean 2017a). Here the integration parameters are $\beta_{int} = 0.256$ and $\gamma_{int} = 0.505$ which adds small amounts of artificial damping to the system in order to reach convergence earlier. This artificial damping has negligible effect on the final results.

In OrcaFlex the implicit Generalized-α integration scheme is used. This method also adds small amounts of numerical damping to the system in order to damp out the non-physical high-frequency part of the response inherent in the FEM solution procedure (Orcina 2018). Again, this added damping has close to no effect on the final solution.

Several steps have been taken to stabilize the time-domain solution in both computer programs. To reduce the effect of transients in the results a ramping time of 100 seconds is used and the initial 1,000 seconds are removed from the response time series in the post-analysis. The time steps used in the two computer programs are based on individual time step convergence studies. SIMO-RIFLEX uses a time step of 0.01 seconds, whereas OrcaFlex uses 0.2. To compensate for this difference the SIMO-RIFLEX time series are down sampled to a time step of 0.2 before comparing standard deviations, response spectra and so forth.

Program Comparison Method

The static response and the modal properties given by the two computer programs are compared, and subsequently several comparisons are made between time domain results. The comparison in the time domain includes deterministic response from regular long-crested waves, followed by six stochastic load cases listed in Table 4. The load cases are chosen in order to identify the differences in the response for each step of complexity added in the models. Starting with first order long-crested irregular wave loads and no viscous effects from the heave plate (LC1), the comparison follows two paths; A) Directional spreading is included in two different ways (LC2a and LC2b) and later viscous effects from the heave plate are added (LC3). B) Second order long-crested irregular wave loads are added (LC4) and finally viscous effects from the heave plate is added (LC5). The JONSWAP wave parameters specified for each load case are chosen according to the 100-year wave environment at the Bjørnafjorden site (Statens Vegvesen 2017) for a wave direction of 270°. For each load case six 1-hour simulations with unique sets of wave seeds are used in the analysis in order to have a stable standard deviation of the response. The comparison focuses on the vertical displacement and the bending moments along the bridge

RESULTS AND DISCUSSION

Static Response of Floating Bridge

Table 5 shows a selection of the static response along the bridge girder in calm water based on the same stiffness and mass input for the bridge superstructure and the pontoons. The two computer programs generally show the same results but small differences are present. An increasing difference in the vertical displacement z from AX3 to AX8 is noted between the two computer programs, with differences starting at 0.03 % (1.5 cm) and steadily increasing to 0.87 % (13.0 cm). The increasing difference is a result of SIMO-RIFLEX exhibiting increasingly smaller values along the high bridge section. At the low bridge section from AX8 to AX21 the difference is constant at roughly 0.87 % (13.0 cm). The weak axis bending moment shows a slight difference of up to 7 % (60 MNm) between the two computer programs noting that SIMO-RIFLEX consistently gives larger negative values along the bridge. The effective tension T_e varies along the bridge with positive values between 300 and 800 kN at AX3 to AX7 in OrcaFlex. At the same locations SIMO-RIFLEX show roughly 35 % larger positive (tension) values. At the low bridge section from AX8 to AX21 OrcaFlex show negative tension of roughly -250 kN whereas SIMO-RIFLEX show slightly positive tension around 40 kN. Although these differences are small they are thought to have an effect on the natural frequencies and modeshapes in the two computer programs.

Natural Frequencies and Modeshapes

Table 6 lists the natural periods found using the two computer programs and an indication of the dominating motions for the corresponding modeshapes. The natural periods T_n are found using the added mass at infinite frequency when solving the standard eigenvalue problem, whereas T_n^a values are found by using the pseudo procedure listed in Tab. 3 for SIMO-RIFLEX. Natural periods denoted by T_n^b are found manually using OrcaFlex and the graphical method described above.

An initial observation is the significance influence of the frequency-dependent added mass on the estimated natural periods. Due to the heave plate the frequency-dependent part of the added mass has a significant influence and should not be neglected.

In general the first eight natural periods T_n have distinct values separated with a large margin and their corresponding modeshapes are primarily in the horizontal plane and has secondary torsional motions. From mode eight and upwards the difference in the values are less than a second and for the most part less than roughly 0.3 seconds. The lower natural periods will be excited by both first and second order wave loads, while the higher natural periods coincide with the wave spectrum at the Bjørnafjorden site resulting in roughly 35 active modeshapes to be accounted for in the design. The higher modes are important since the dominating motions are in the vertical plane and include pendulum motion of the pontoons. Both of these increase the weak axis bending moment in the bridge girder significantly.

A reasonable match within 2% is noted between most of the natural periods in the two computer programs, with only mode 3, 6 and 7 having differences of 3.8, 4.9 and 4.1%, respectively. Although natural periods T_n^a are given for the pseudo procedure shown in Tab. 3 they will not be compared to the natural periods T_n^b using the graphical method due to fundamental differences in the two methods. Instead the T_n^a values will later be used to link the natural periods to the response spectra.

As the natural periods differ slightly so do the corresponding modeshapes shown in Fig. 5. The first six modes show the same form but as the modes increase so do the differences between the two computer programs. Mode 10 to 28 all show the same general shapes with increasing dominance of the vertical and pendulum motion. OrcaFlex seems to emphasise the horizontal and torsional motion more than SIMO-RIFLEX. This can have important effects on the dynamic response of the bridge in general. The differences observed in the natural periods are thought to be related to the small deviations in the static response, possible rounding errors and more generally a difference in the implementation of the theory in the two computer programs. With mass and stiffness being the only governing parameters for the value of the natural periods of the structure, the difference is to be found in either erroneous mass and stiffness input by the users of the two computer programs, or the implemented methods governing the calculation of the natural periods inside the two computer programs. We have made our best effort to compensate for the differences in the implementation of the theory in the two computer programs and checked the input on several different occasions to eliminate any possible user mistakes. A potential user mistake is how the rotational mass is included in the two computer programs. In OrcaFlex the rotational mass is included using 6 DOF Buoys at each element node along the bridge elements. These 6 DOF Buoys are only given rotational mass properties and have no other effect on the model. In SIMO-RIFLEX it is included as a constant radius of gyration value r_x for each cross-section. The values are linked through Eqn. 9.

$$r_x = \sqrt{\frac{R_x}{m \cdot L_e}} \tag{9}$$

Where r_x is the radius of gyration used in SIMO-RIFLEX, R_x is the total moment of inertia of the 6 DOF Buoy, m is the average mass per meter of the adjacent elements and L_e is the average element length. As the 6 DOF Buoys are attached to the element nodes a sensitivity study has been carried out internally regarding the needed distance between the Buoys. The findings suggest that the 10 m used in the present paper is a sufficient length. Based on this procedure, the differences observed in the natural periods are thought to be related to how the two computer programs implement the theory governing the calculation of the natural periods, including the used of the final static position in the Generalized Lanczos Method when calculating the natural periods. It is particularly the rotational modes that are shown to be the most uncertain and further experimental verification is needed before any concluding remarks can be made regarding this issue. A validation towards old experiments for a short floating bridge structure has been carried out in Xiang and Løken (2019) for OrcaFlex and a similar verification is currently under way for SIMO-RIFLEX. However, the shorter bridge has very different dynamic properties with the lowest natural period of approximately 10 s. Furthermore, in order to verify the numerical models of the presented long floating bridge structure, only a part of the bridge can be compared due to size limitations of existing ocean basins and hybrid tests are the only option. This forces the experimental results to rely heavily on the computer program used. The issue with the rotational modes highlighted here is hence an important contribution and sheds light on the need for including model tests aimed at the issue with rotation.

Dynamic Response in Regular Waves

This section describes the deterministic response from regular long-crested waves. Figure 6 illustrates the dynamic vertical motion of the bridge girder at AX11 calculated using the two computer programs showing an insignificant variation in the amplitude and period. Initial transients are observed in both computer programs up to roughly 1,000 seconds depending on the wave period but eventually a stable steady state response is found.

The response amplitude operator (RAO) of the vertical displacement z, the weak axis bending moment M_y and the strong axis bending moment M_z are illustrated in Fig. 7 with the chosen locations representing the general behaviour along the bridge. The natural periods T_n^a from SIMO-RIFLEX using the iterative method are also shown in the figure for mode 4, 5, 6, 10 and 28 in order to illustrate the connection to the relevant modeshapes.

The two computer programs show a satisfactory agreement with some differences at AX10 for the weak axis bending moment. Generally the RAOs for the vertical displacement in the two computer programs follow the same behaviour. The most dominating peak in the vertical displacement RAO located at 11 s is recurring at almost every pontoon and is explained by roughly six vertical modeshapes being active at natural periods within 1 s away from this peak. For OrcaFlex two additional peaks are shown at roughly 15 s (mode 5) and 19 s (mode 4) for AX10, AX15 and AX20. This peak is not represented in SIMO-RIFLEX which seems to be related to the different shape of mode 4 and 5 in the two computer programs.

The strong axis bending moment in the bridge girder exhibits similar trends in the RAOs with some notable shifts in the peak periods, corresponding to the slight differences in the periods of mode 4 and 5 representing horizontal modes. The amplitudes at the corresponding peaks show a satisfactory agreement.

The RAOs for the weak axis bending moment are less similar in shape but are within the same order of magnitude. The complexity of the system makes it difficult to explain the exact reasons but some general comments can be given about the behaviour. In both computer programs the weak axis bending moment RAOs seem to be governed primarily by high frequency modes around mode 28, except for the bridge ends (here illustrated with the RAOs at AX5 and AX20), where the energy at low frequency modeshapes is significantly larger. In OrcaFlex the three dominating peaks at AX5 are strongly correlated to mode 4, 5 and 7. The same peaks are also present at the low bridge section, although with significantly smaller amplitudes. Instead the frequencies around mode 10 and 28 are relatively more important. Using the same analogy for SIMO-RIFLEX, the dominating frequencies are close to mode 4, 5, 6, 10 and 28, albeit the correlation is not as strong as in OrcaFlex.

The structural system is not only complex due to the close modeshapes but also directionality sensitivity is a large contributor. Figure 8 shows the RAOs at AX5 with a resolution of 1 second in OrcaFlex for three different wave directions. Waves travelling in directions larger than 270° are more aligned with the longitudinal direction of the bridge girder at AX5 and will generate larger wave forces in surge on the pontoons resulting in higher excitation of the pendulum motion in the bridge girder. This increases the weak axis bending moment as seen in the figure. Similarly the changing wave direction affects the vertical displacement and the strong axis bending moment along the bridge. This effect is captured by both computer programs with only small differences that can be explained by the same source of errors as mentioned above. The directional sensitivity has been reported for similar floating bridges with varying lengths, see e.g. Leira and Remseth (1990), Kvåle et al. (2016), Villoria (2016) and Viuff et al. (2019), and is in part a consequence of the many different modeshapes of the structure.

It should be noted that the mentioned RAOs are found using the time domain method and will not show the same behaviour as results found using the frequency domain method. However, no frequency domain method is available in SIMO-RIFLEX and instead the RAOs include effects apparent in the non-linear time domain solution procedure and imperfect wave loads from the FFT method.

Dynamic Response in Long-crested Irregular Waves

The wind driven waves are governed by the JONSWAP wave spectrum with a peak period of 5.9 s and with the most significant part of the wave energy between 2 and 12 s. The response is therefore governed mostly by the higher modes from 7 and upwards where generally speaking the differences in the RAOs are smaller. However, these higher modes are also the ones showing the largest differences in their corresponding modeshapes.

Figure 9 illustrates variation of the average absolute differences in the standard deviation of the vertical displacement, the effective tension and the weak axis bending moment at the specific axis locations along the bridge based on the six stochastic time domain simulations for load case LC1. The difference in each response change along the entire bridge with each response having minimum and maximum differences at different axes. The average absolute differences along the bridge of the vertical displacement, the effective tension and the weak axis bending moment are roughly 7, 13 and 9%, respectively.

Effect of Directional Spreading

Including directional spreading is a better representation of the wave environment at the Bjørnafjord site and the response spectra of the weak axis bending moment at AX4 and AX11 for load case LC1 and LC2b for both computer programs are shown in Fig. 10. The weak axis bending moment response spectra at the axes generally become more narrow-banded when going from the bridge ends towards the middle of the bridge but the same differences between the two computer programs are present at all locations. The two computer programs capture roughly the same total energy in the weak axis bending moment response spectra but the amplitudes at the different frequencies are not the same, which is again thought to be a consequence of the slight differences in the modal properties for the two computer programs. The directional spreading of the waves increases the number of active modeshapes and in this case for AX4 and AX11 the response spectra for the weak axis bending moment show an increased energy which is also supported by the study by Langen and Sigbjörnsson (1980). Interestingly enough, the two computer programs do not have the same distribution of the energy over the wave frequencies.

Effect of Second Order Wave Loads

For the investigated wave direction, the effect from the second order wave load on the vertical displacement and the weak axis bending moment is negligible. This is expected since the vertical mean drift loads have been omitted in the present study. Instead the transverse displacement along the bridge is increased significantly. Figure 11 shows the response spectrum of the transverse displacement in the global y-direction at AX19, and shows four clear peaks for both software, indicating the natural period of the first four modes of the bridge. The modes shown in the response spectra are close to the predicted values (within 10%).

Another effect seen in Fig. 11 is the increased standard deviation of the transverse displacement along the bridge. The transverse displacement in OrcaFlex is slightly larger, especially close to the high bridge, but with statistical uncertainties they compare well.

Influence From Viscous Effects

The effect of the heave plate on the pontoon is two-fold; to increase the added mass of the bridge and thereby shifting important modes away from the wave spectrum, and to increase the viscous drag on the pontoon in order to damp out the vertical motion and thereby decrease the weak axis bending moment (Xiang et al. 2017).

In the present study the viscous effect is added in two separate steps, between LC2b and LC3 and between LC4 and LC5, to see its effect on the response from short-crested first order wave loads and unidirectional first and second order wave loads, respectively.

With the vertical drag coefficients and the corresponding cross-sectional area being relatively larger than those for the horizontal directions, the viscous effect seen on the responses from short-crested first order wave loads is mainly present in the the vertical responses as seen in Fig. 12 for the vertical motion with an average reduction of roughly 8%. A similar average reduction is present in the weak axis bending moment and overall the same effects are captured in both software when including viscous drag.

The viscous effect on the response from the unidirectional first and second order wave loads is mainly seen in the horizontal response with a reduction in the horizontal motion and effective tension of roughly 20 and 14%, respectively, at almost all axes for OrcaFlex. On average the corresponding values for SIMO-RIFLEX are roughly 7-10% larger. The effect on the strong axis bending moment is shown in Fig. 12 where an average reduction of roughly 7% is present for OrcaFlex, although the actual effect at each axis varies along the bridge. For almost all axes SIMO-RIFLEX shows an increased 5% reduction. The vertical response is also affected, although the effect is much smaller. Negative damping shown as a negative reduction (increase in response) is present at some axes in both software for the vertical motion and the weak axis bending moment, although in OrcaFlex this effect is larger and located at more axes.

Final Notes on Averaged Differences

The standard deviation of the different responses serves to quantify the response along the bridge girder in the two computer programs. As a benchmark of the comparison, averaged absolute differences in the standard deviations of the response along the bridge can be applied. Equation (10) shows how these averaged differences are calculated:

$$\mathrm{STD_{Diff}} = \frac{1}{N_p}\sum_{p=1}^{N_p}\left(\frac{|\mathrm{STD_{SIMO\text{-}RIFLEX}} - \mathrm{STD_{OrcaFlex}}|}{\mathrm{STD_{OrcaFlex}}}\right) \tag{10}$$

where N_p is the number of pontoons. Figure 13 shows box plots of the differences in the internal forces M_y, M_z and T_e in the bridge girder above the 19 pontoon locations along the bridge with the $\times$ representing the averaged difference along all the axes for each response type. Furthermore, the horizontal line indicate the median (located at AX12), the two ends show the minimum and maximum differences and the ends of the box indicate the 50% quantiles. The weak and strong axis bending moments are among the main contributors to the normal stresses in the design of the bridge girder and existing differences will have a significant influence on the final design.

For load case LC1 the average difference in the stochastic response is within 5 and 15%, which is thought to be a realistic benchmark. When comparing the response for short-crested waves however, care must be given to modelling exactly the same directional spreading function $D(\theta)$

in the two computer programs. In SIMO-RIFLEX the spreading angles are by default linearly distributed from $-\frac{\pi}{2}$ to $\frac{\pi}{2}$, whereas in OrcaFlex the spreading angles are weighted according to an equal energy strategy (Orcina 2018). In Fig. 13 load case LC2a uses the default modelling in both computer programs, whereas in load case LC2b the numerical values for the directional spreading function in OrcaFlex are given as manual input to SIMO-RIFLEX, resulting in significant differences in the average standard deviation for the weak axis bending moment. These larger values for LC2a is due to the larger portion of the waves hitting the pontoons from the side and hence increasing the bridge girder weak axis bending moment. Taking care of modelling exactly the same wave load input in the two computer programs the differences are down to less than 10%. These differences are to some extent directly linked to the general complexity of the system amplifying any small modelling differences when calculating the global response. On top of this, modelling of the boundary conditions, pre-tension forces, methods for implementation of the wave loads and definition of the mass properties of the bridge girder elements are all influencing factors on the final modeshapes and thereby the different stochastic response characteristics. In our experience, if it is not possible to obtain natural periods within less than 5% from each other and having the same modeshapes, it will influence the comparison of any RAOs or stochastic response of the floating bridge structure due to the high complexity. Particularly the uncertainty in the rotational modes is thought to have an effect on the stochastic response. Furthermore different methods for including artificial damping and differences in the solution algorithms also contribute to the variations between the two computer programs.

When comparing the differences in the response for unidirectional first and second order wave loads (LC4), the weak and strong axis bending moment are both close to 10% from each other. Some larger differences are observed in the effective tension along the bridge axes between 5-25% with an average of 20%. However, these standard deviations are observed to fluctuate up to 20% from the average within the six simulated time series due to the strong dependency on the randomly generated wave seed.

Including viscous drag using Morison elements in the two models (LC3 and LC5) it seems that the previously listed sources of error are both amplified and reduced by the positive and negative damping, respectively.

CONCLUDING REMARKS

An extensive software-to-software comparison of the dynamic characteristics of an end-anchored floating pontoon bridge is presented. The comparison includes natural frequencies, regular long-crested wave response, response amplitude operators (RAOs), first and second order long-crested stochastic waves, directional spreading and viscous effects of the pontoon heave plate. The responses compared in the two computer programs are the vertical and horizontal displacement, effective tension and weak and strong axis bending moments in the bridge girder.

The natural frequencies compared are based on results from solving the standard eigenvalue problem and show differences below 5%. Noticeable differences in the modeshapes are observed between the two computer programs related to longitudinal rotation of the bridge. The differences are thought to be related to software differences in the implemented methods governing the calculation of the static response, natural frequencies and modeshapes. Particularly the uncertainty in the rotational modes is an important finding and needs further investigation using model tests.

Good agreement between the two computer programs is found for the vertical displacement RAOs along the bridge girder. The peaks in the weak and strong axis bending moment RAOs follow the modal properties of each program and the comparison between the two computer programs is strongly influenced by small differences in their respective modal properties.

Special care was taken when modelling the directional spreading function in the two computer programs. Different methods are by default applied in the two computer programs when distributing the wave direction angles in the spreading function, and an exact replica of the OrcaFlex spreading function was manually specified in SIMO-RIFLEX. The difference in the comparison with default and manual settings are roughly 20% for the average standard deviation of the weak axis bending moment along the bridge.

The effect of second order wave loads are captured well in both computer programs where only the horizontal displacement and the strong axis bending moment are influenced. The first four natural frequencies are captured in the horizontal displacement response spectrum and agree well with the natural frequencies found using the iterative approach.

Including viscous effects in the two computer programs reduces the differences in the weak axis bending moment and can hide potential modelling errors.

Based on the findings in the present paper any future hybrid model tests should expect uncertainties between the mentioned software of roughly 5-15% depending on the response type.

DATA AVAILABILITY STATEMENT

Some or all data, models, or code generated or used during the study are available from the corresponding author by request. These items are specifically software input files and result values shown in the present paper.

ACKNOWLEDGEMENTS

This research was carried out with financial support from the Coastal Highway Route E39 Project of the Norwegian Public Roads Administration. The authors greatly acknowledge this support.

REFERENCES

Cheng, Z., Gao, Z., and Moan, T. (2018a). "Hydrodynamic load modeling and analysis of a floating bridge in homogeneous wave conditions." *Marine Structures*, 59, 122–141.

Cheng, Z., Gao, Z., and Moan, T. (2018b). "Numerical modeling and dynamic analysis of a floating bridge subjected to wind, wave, and current loads." *Journal of Offshore Mechanics and Arctic Engineering*, ASME, 141.

Cheng, Z., Gao, Z., and Moan, T. (2018c). "Wave load effect analysis of a floating bridge in a fjord considering inhomogeneous wave conditions." *Journal of Engineering Structures*, 163, 197–214.

Cummins, W. E. (1962). *The impulse response function and ship motions*. Washington D.C., USA. Report no. DTMB-1661.

DNV (2014). *Wadam - Wave analysis by diffraction and morison theory, SESAM user Manual*. Høvik, Norway. Report no. 94-7100.

Faltinsen, O. M. (1993). *Sea loads on ships and offshore structures*. Cambridge University Press.

Fu, S., Wei, W., Ou, S., Moan, T., Deng, S., and Lie, H. (2017). "A time-domain method for hydroelastic analysis of floating bridges in inhomogeneous waves." Vol. Volume 9: Offshore Geotechnics; Torgeir Moan Honoring Symposium of *International Conference on Offshore Mechanics and Arctic Engineering*, ASME, 1–8 (09).

Hasselmann, K., Barnett, T. P., Bouws, E., Carlson, H., Cartwright, D. E., Enke, K., Ewing, J. A., Gienapp, H., Hasselmann, D. E., Kruseman, P., Meerburg, A., Muller, P., Olbers, D. J., Richter, K., Sell, W., and Walden, H. (1973). "Measurements of Wind-Wave Growth and Swell Decay during the Joint North Sea Wave Project (JONSWAP)." *Deutsche Hydrographische Zeitschrift*, 8.

Karimirad, M., Meissonnier, Q., Gao, Z., and Moan, T. (2011). "Hydroelastic code-to-code comparison for a tension leg spar-type floating wind turbine." *Marine Structures*, 24, 412–435.

Kvåle, K. A., Sigbjörnsson, R., and Øiseth, O. (2016). "Modelling the stochastic dynamic behaviour of a pontoon bridge: A case study." *Computers and Structures*, 165, 123–135.

Langen, I. and Sigbjörnsson, R. (1980). "On stochastic dynamics of floating bridges." *Engineering Structures*, 2(4), 209–216.

Leira, B. J. and Remseth, S. (1990). "Directional effects and multicomponent dynamic response of marine bridges." *Proceedings of the 2nd Symposium on Strait Crossings*, Balkema Publishers Rotterdam, 233–239.

Løken, A. E. and Oftedal, R. A. (1990). "Aspects of hydrodynamic loading and response in design of floating bridges." *Second Symposium on Strait Crossings*, 479–486.

Orcina (2018). *OrcaFlex Documentation*. Online Manual.

Pan, Z. Y., Vada, T., and Hanssen, F.-C. W. (2013). "A mesh dependency study for the mean drift forces by pressure integration." *Proceedings of the 32nd International Conference on Ocean, Offshore and Arctic Engineering*, ASME, Nantes, France.

Robertson, A., Jonkman, J., Vorpahl, F., Popko, W., Qvist, J., Frøyd, L., Chen, X., Azcona, J., Uzunoglu, E., Soares, C. G., Luan, C., Yutong, H., Pengcheng, F., Yde, A., Larsen, T., Nichols, J., Buils, R., Lei, L., Nygaard, T. A., Manolas, D., Heege, A., Vatne, S. R., Ormberg, H., Duarte, T., Godreau, C., Hansen, H. F., Nielsen, A. W., Riber, H., Cunff, C. L., Beyer, F., Yamaguchi, A., Jung, K. J., Shin, H., Shi, W., Park, H., Alves, M., and Guérinel, M. (2014). "Offshore code comparison collaboration continuation within iea wind task 30: Phase ii results regarding a floating semisubmersible wind system." *Proceedings of the 33rd International Conference on Ocean, Offshore and Arctic Engineering*, ASME.

Shao, Y.-l., You, J., and Glomnes, E. B. (2016). "Stochastic linearization and its application in motion analysis of cylindrical floating structure with bilge box." *Proceedings of the 35th International Conference on Ocean, Offshore and Arctic Engineering*, ASME, Busan, South Korea.

SINTEF Ocean (2017a). *RIFLEX 4.10.0 Theory Manual*. Trondheim, Norway.

SINTEF Ocean (2017b). *SIMO 4.10.0 Theory Manual*. Trondheim, Norway.

Stansberg, C. T., Ormberg, H., and Oritsland, O. (2002). "Challenges in deep water experiments: Hybrid approach." *Journal of Offshore Mechanics and Arctic Engineering*, ASME, 124, 90–96.

Statens Vegvesen (2016). *Curved bridge navigation channel in south - environmental loading analyses*. Oslo, Norway. Report no. NOT-HYDA-018.

Statens Vegvesen (2017). *Hydrodynamic model tests specification - Floating Bridge Pontoons*. Oslo, Norway. Report no. SBJ-20-C3-SVV-21-TN-002.

Sørum, S. H., Horn, J.-T. H., and Amdahl, J. (2017). "Comparison of numerical response predictions for a bottom-fixed offshore wind turbine." *Energy Procedia*, 137, 89–99.

Tao, L. and Cai, S. (2004). "Heave motion suppression of a spar with a heave plate." *Ocean Engineering*, 31, 669–692.

Villoria, B. (2016). "Floating bridge technology - prediction of extreme environmental load effects." *Proceedings of the 35th International Conference on Ocean, Offshore and Arctic Engineering*, ASME, 1–8.

Viuff, T., Leira, B. J., Xiang, X., and Øiseth, O. (2019). "Effects of wave directionality on extreme response for a long end-anchored floating bridge." *Journal of Applied Ocean Research*, 90.

Viuff, T., Xiang, X., Leira, B. J., and Øiseth, O. (2018). "Code-to-code verification of end-anchored floating bridge global analysis." *Proceedings of the 37th International Conference on Offshore Mechanics and Arctic Engineering*, 1–9.

Xiang, X. and Løken, A. (2019). "Hydroelastic analysis and validation of an end-anchored floating bridge under wave and current loads." *Proceedings of the 38th International Conference on Offshore Mechanics and Arctic Engineering*, ASME, 1–9.

Xiang, X., Svangstu, E., Nedrebø, Ø., Jakobsen, B., Eidem, M. E., Larsen, P. N., and Sørby, B. (2017). "Viscous damping modelling of floating bridge pontoons with heaving skirt and its impact on bridge girder bending moments." *Proceedings of the 36th International Conference on Ocean, Offshore and Arctic Engineering*, ASME, 1–10.

List of Tables

TABLE 1. Properties of bridge girder cross-sections (Statens Vegvesen 2017). The bending stiffness about the weak and strong girder axis is denoted by EI_y and EI_z, respectively. The torsional stiffness and the radius of gyration are denoted by GI_x and r_x respectively.

		H1	H2	H3	S1	F1
Mass	[ton/m]	2.40E+01	2.91E+01	3.31E+01	3.18E+01	2.67E+01
r_x	[m]	1.66E+01	1.73E+01	1.76E+01	1.82E+01	1.76E+01
EA	[kN]	3.06E+08	4.41E+08	5.51E+08	5.25E+08	3.89E+08
EI_y	[kNm^2]	1.28E+09	1.98E+09	2.48E+09	3.85E+09	2.77E+09
EI_z	[kN^2]	1.16E+11	1.70E+11	2.12E+11	2.18E+11	1.55E+11
GI_x	[kN^2/rad]	1.42E+09	1.98E+09	2.48E+09	3.70E+09	2.90E+09

TABLE 2. Pontoon properties without ballast (Statens Vegvesen 2017)

Property	Unit	Value
Mass	[ton]	1.13E+04
Roll inertia	[ton·m^2]	4.90E+06
Pitch inertia	[ton·m^2]	1.36E+06
Yaw inertia	[ton·m^2]	5.70E+06
COG from waterline	[m]	-4.20E+00
Displacement	[ton]	1.88E+04
Roll water plane stiffness	[kNm/rad]	3.98E+06
Pitch water plane stiffness	[kNm/rad]	7.38E+05
Heave stiffness	[kN/m]	1.74E+04

TABLE 3. Pseudo procedure to solve the standard eigenvalue problem when manually including frequency-dependent added mass

INPUT N, $A(\omega)$, tolerance
Solve $\left[\mathbf{K} - \omega^2(\mathbf{M} + \mathbf{A}^{\infty})\right]\psi = 0$
Store the first N natural frequencies as ω_n
FOR $n = 1$ to N
    $\omega_{out} = \omega_n$
    diff = tolerance + 1
    WHILE diff > tolerance
        $\omega_{in} = \omega_{out}$
        Solve $\left[\mathbf{K} - \omega^2(\mathbf{M} + \mathbf{A}(\omega_{in}))\right]\psi = 0$
        Store the n'th natural frequency as ω_{out}
        diff = $|\omega_{in} - \omega_{out}|$
    END
    Store ω_{out} as ω_n^a
END

TABLE 4. Load cases with irregular waves used in the present study with a main wave direction of 270° and JONSWAP parameters H_s = 2.4 m, T_p = 5.9 s and γ = 2.0. Load case LC2a and LC2b include 11 wave directions in the directional spreading function distributed according to the default of each program (LC2a) and by manually specifying the exact same directions in SIMO-RIFLEX as in OrcaFlex (LC2b).

Load Case	Waves Loads	Viscous Effects	Spreading
LC1	1^{st} order	No	-
LC2a	1^{st} order	No	4
LC2b	1^{st} order	No	4
LC3	1^{st} order	Yes	4
LC4	1^{st} + 2^{nd} order	No	-
LC5	1^{st} + 2^{nd} order	Yes	-

TABLE 5. Static response at selected locations along the floating bridge

Axis	SIMO-RIFLEX			OrcaFlex		
	z	M_y	T_e	z	M_y	T_e
	[m]	[MNm]	[kN]	[m]	[MNm]	[kN]
AX3	47.5	-532	798	47.4	-521	539
AX4	42.3	-1,000	1,011	42.4	-939	743
AX5	34.7	-856	1,074	34.8	-799	818
AX6	26.8	-898	1,064	27.0	-839	802
AX7	19.0	-889	567	19.1	-830	290
AX8	15.0	-893	57	15.1	-834	-236
AX10	15.0	-895	51	15.1	-835	-244
AX15	15.0	-899	37	15.1	-838	-257
AX20	15.0	-901	21	15.1	-839	-262

TABLE 6. Natural periods of the floating bridge models. The notation T_n indicates the use of added mass at infinite frequency when solving the standard eigenvalue problem. The notations T_n^a and T_n^b indicate the use of the iterative and graphical procedure to include the exact added mass, respectively. The symbols for primary and secondary motions refer to horizontal (H), vertical (V), torsional (T) and pendulum (P) motions. Pendulum motion is the motion of the pontoons going from side to side like a pendulum.

Mode	SIMO-RIFLEX				OrcaFlex				Diff.
n	T_n	T_n^a	Dominating motion		T_n	T_n^b	Dominating motion		T_n
[-]	[s]	[s]	Primary	Secondary	[s]	[s]	Primary	Secondary	[%]
1	50.79	55.63	H	-	51.81	54.15	H	-	2.0
2	29.28	31.63	H	-	29.79	30.64	H	-	1.7
3	22.55	24.41	H	T	21.76	22.79	H	T	3.8
4	17.56	19.28	H	T	17.52	18.53	H	T	0.2
5	13.56	14.91	H	T, V	13.59	14.66	H	T	0.1
6	12.67	13.06	T	H, V	12.08	12.26	H	T	4.9
7	12.15	12.31	V	T	11.67	11.71	H	V	4.1
8	11.44	11.29	T	V	11.39	11.53	V	H	0.5
9	11.39	11.27	V	-	11.37	11.34	V	H, T	0.2
10	11.39	11.09	V	-	11.36	11.16	V	H, T	0.2
17	10.69	9.96	V	P	10.61	-	V	P, H	0.8
24	8.91	9.24	V	P	8.81	-	V	T, P	1.1
28	8.13	8.02	T	H	7.97	-	V	H, V, P	2.0

List of Figures

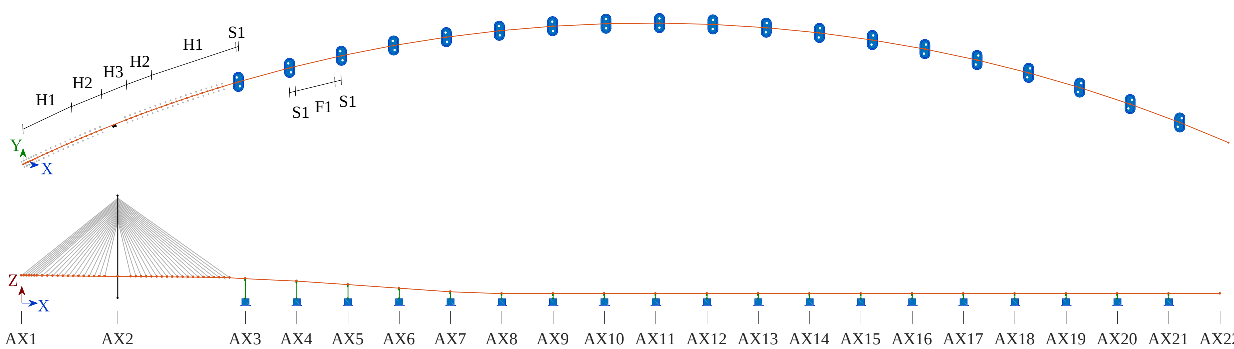

Fig. 1. End-anchored horizontally curved floating pontoon bridge seen from above (top) and the side (bottom)

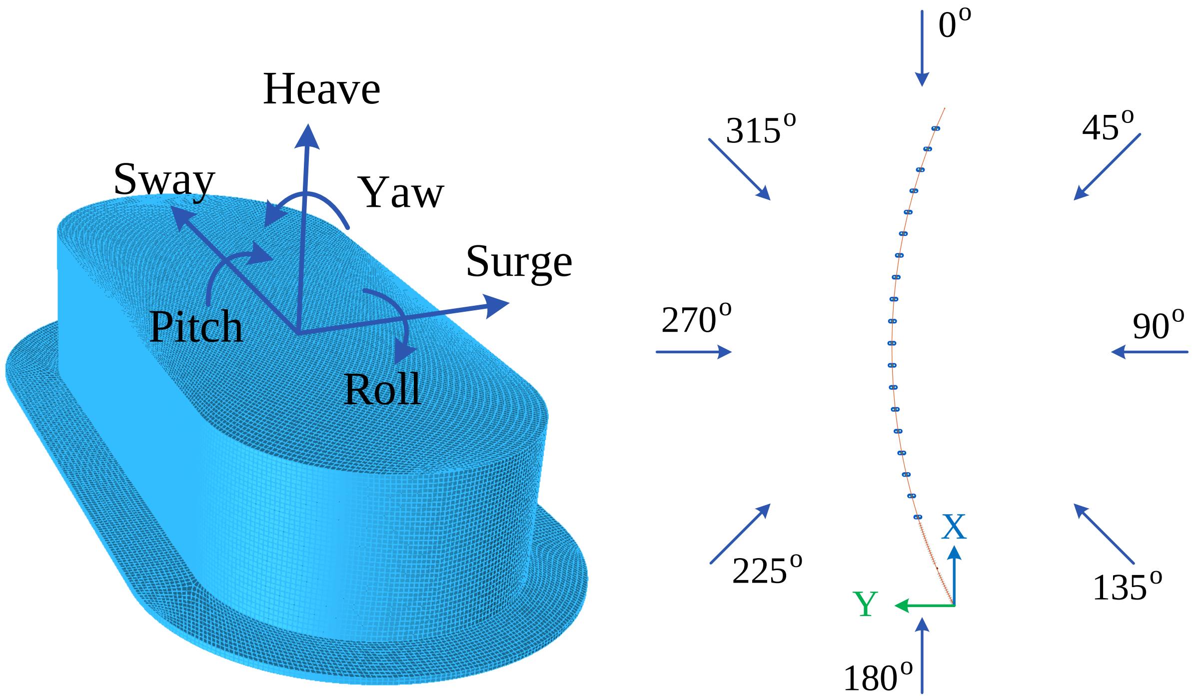

Fig. 2. Pontoon panel model with heave plate extruding from the bottom (left) and compass notation of wave directions at the Bjørnafjord site (right) (Viuff et al. 2018).

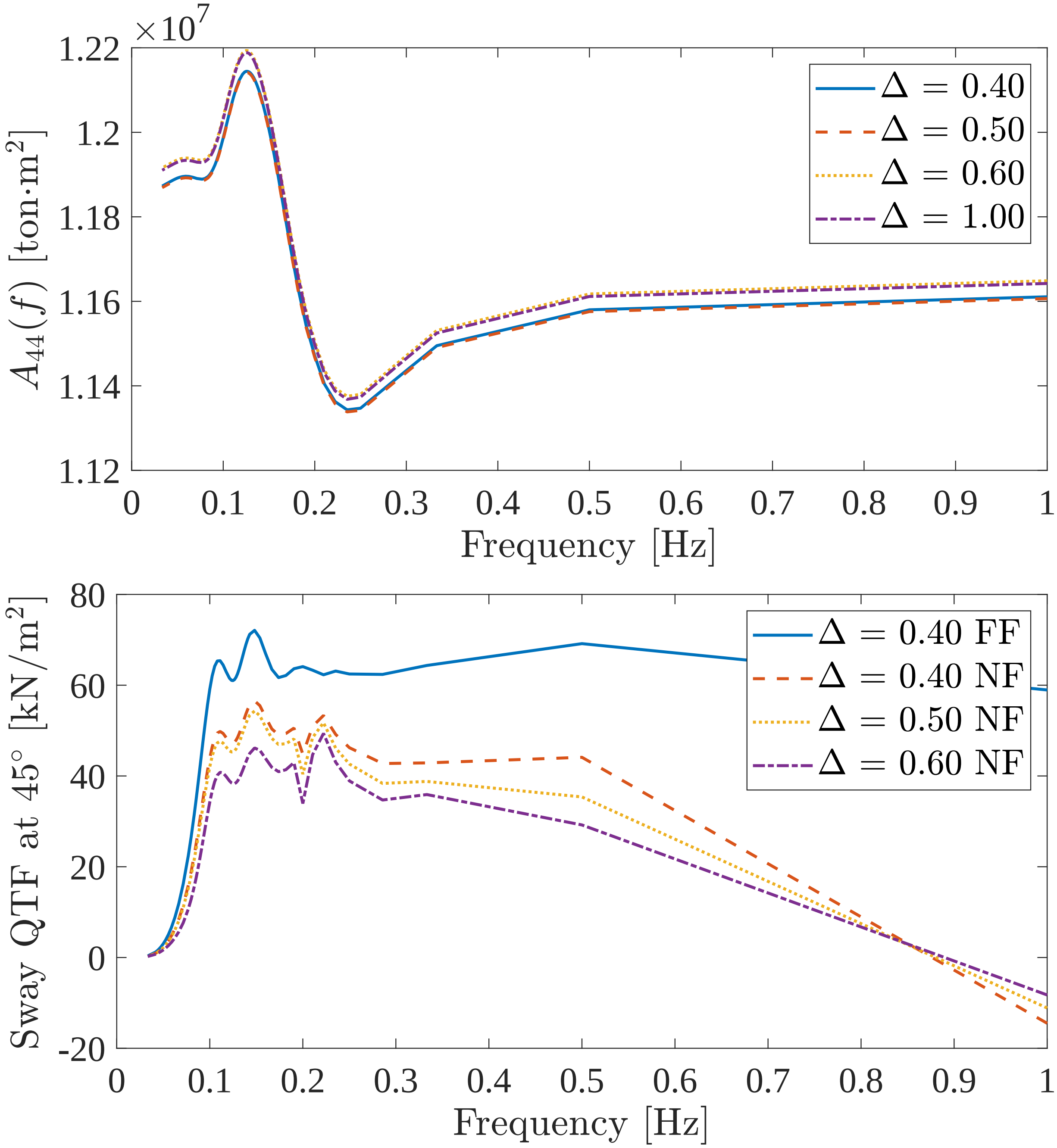

Fig. 3. Convergence with respect to element length Δ in the pontoon panel model. Comparison of total hydrodynamic added mass in roll (top) and of near-field (NF) and far-field (FF) methods for the mean drift load (bottom). For convenience, only a single line is shown for the FF method since the remaining lines, representing the other mesh sizes when using the FF method, are almost identical.

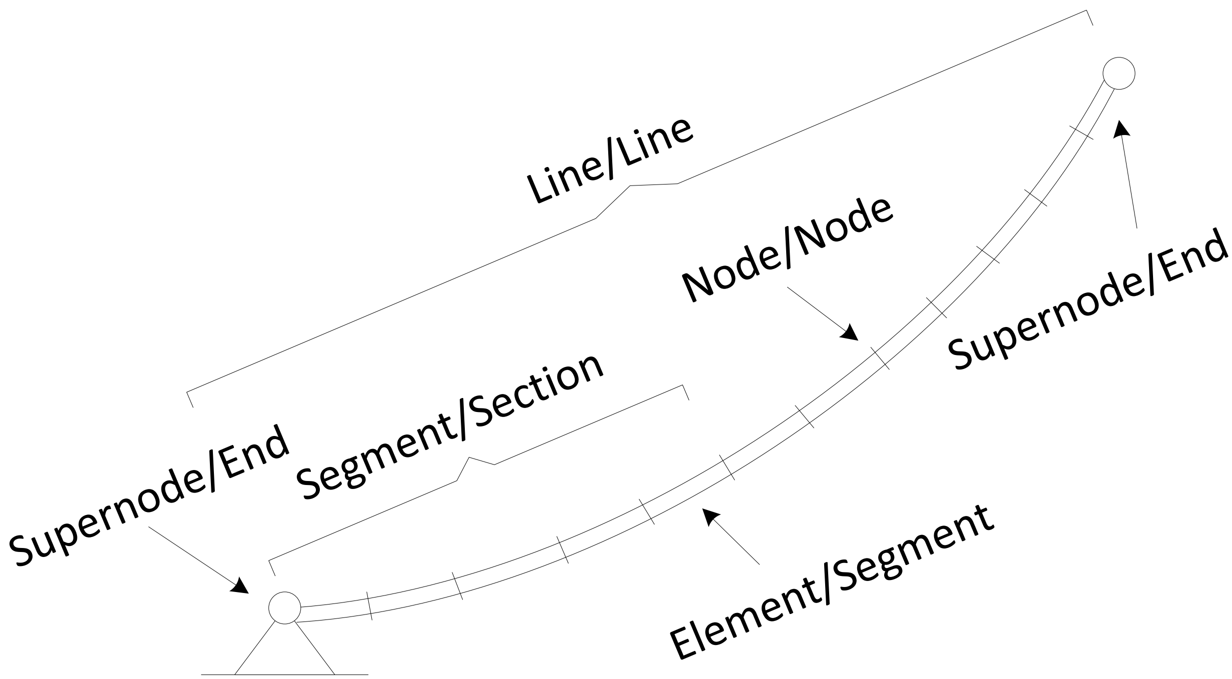

Fig. 4. Sketch of Finite Element model for a line with specified SIMO-RIFLEX/OrcaFlex nomenclature. Sketch inspired by (SINTEF Ocean 2017a).

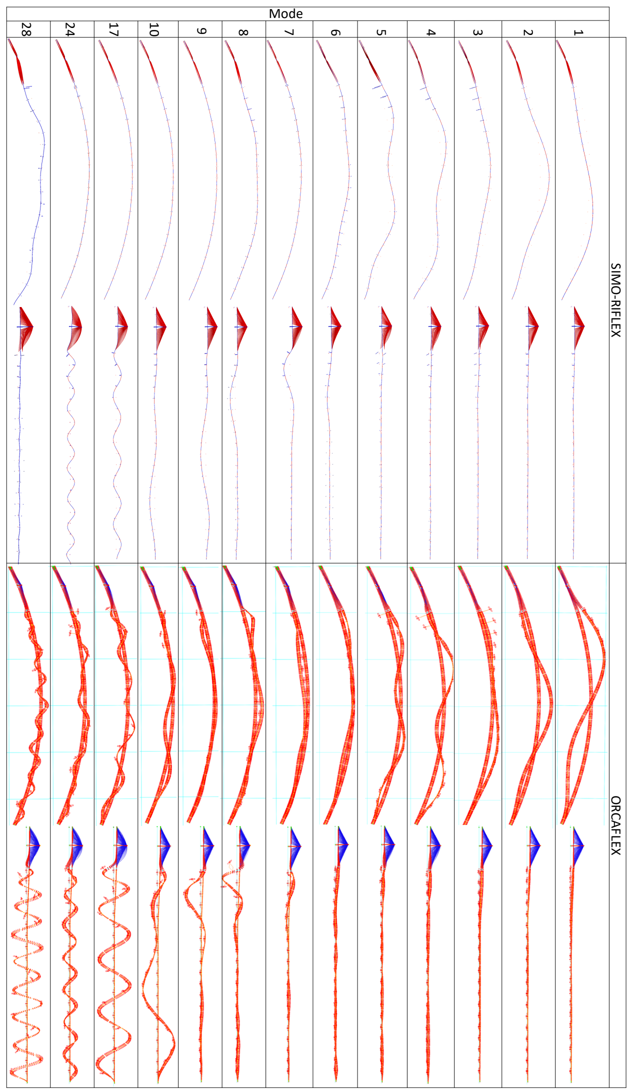

Fig. 5. Modeshapes of floating pontoon bridge using added mass at infinite frequency

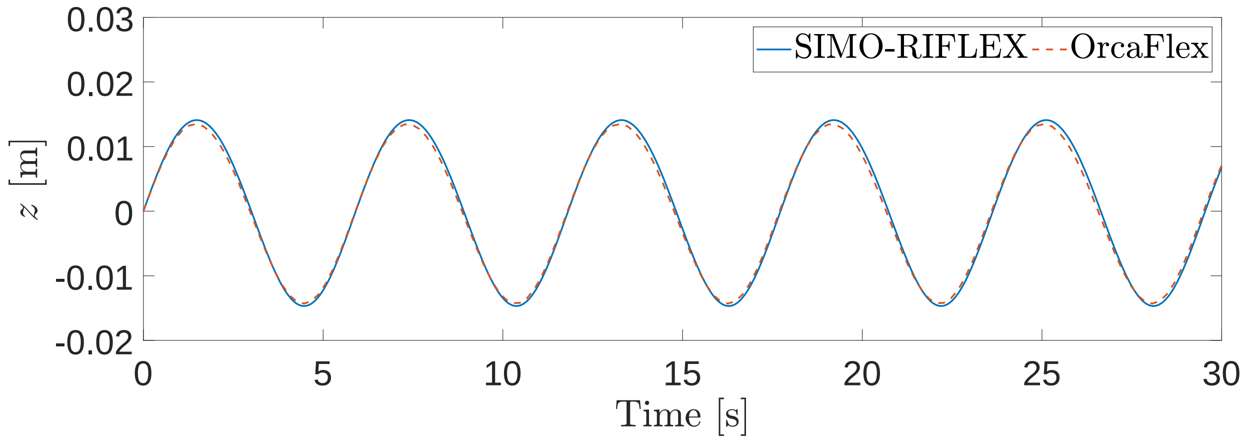

Fig. 6. Dynamic vertical motion of bridge girder at AX11 when subjected to regular long-crested waves from 27° with $T = 5.9$ s and $H = 2.4$ m

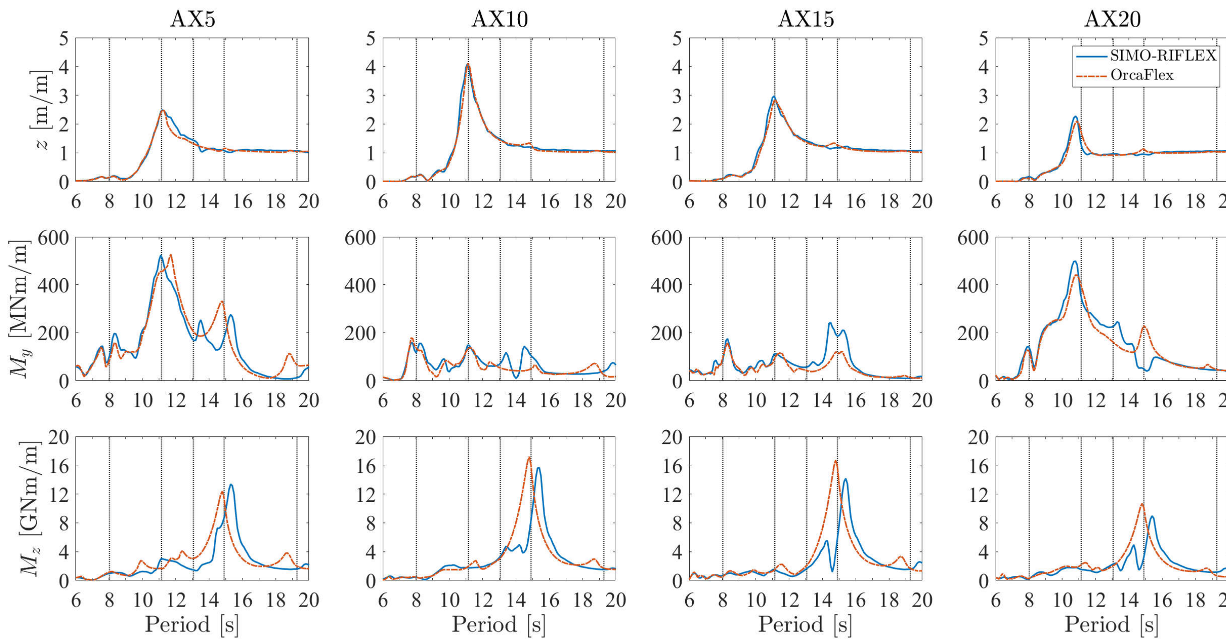

Fig. 7. RAOs at 270° waves for vertical displacement (top), weak axis bending moment (middle) and strong axis bending moment (bottom) at axis AX5, AX10, AX15 and AX20 along the bridge. The natural periods T_n^a based on the iterative method in SIMO-RIFLEX are shown as the vertical dotted lines for mode 4, 5, 6, 10 and 28 from right to left.

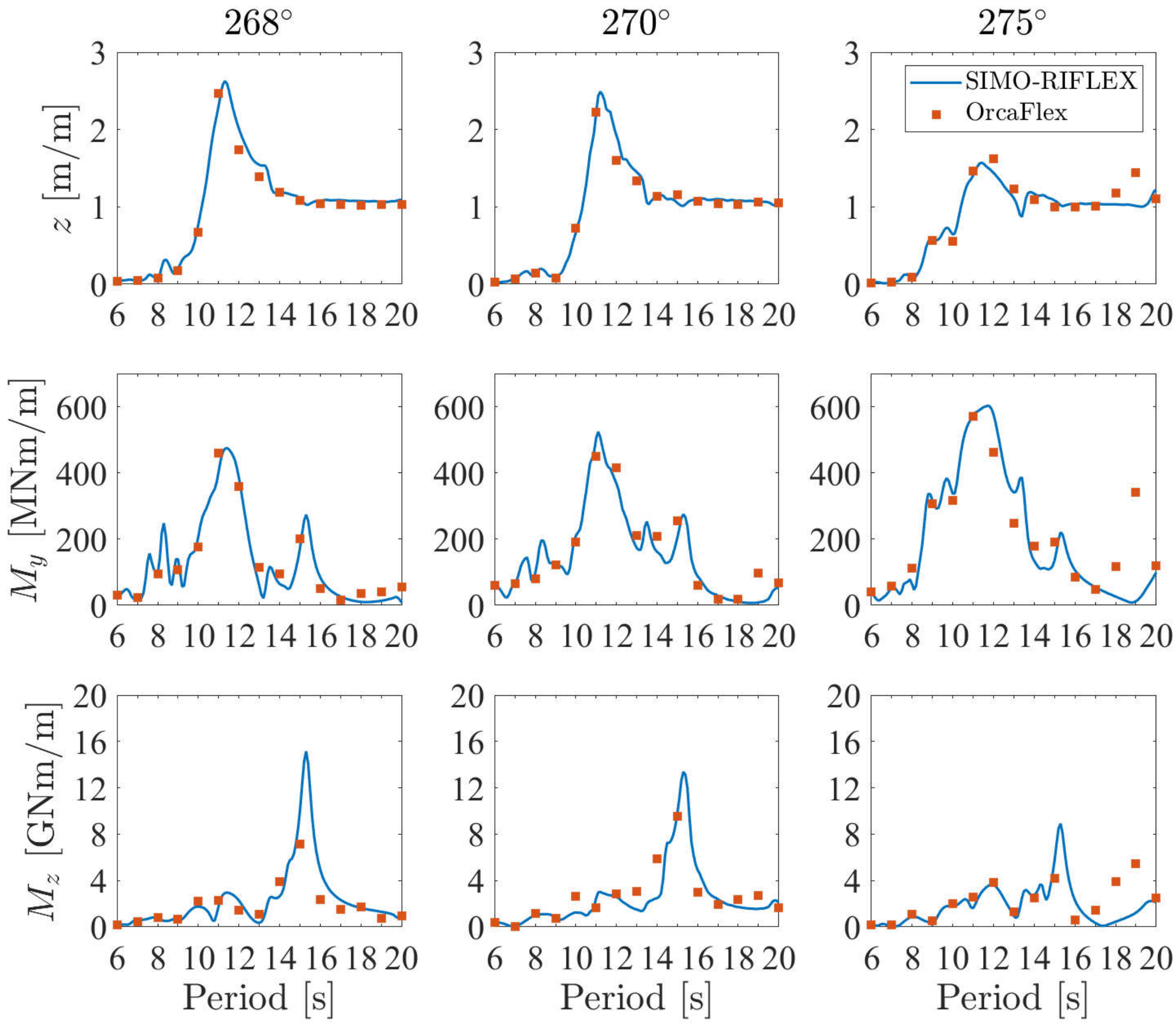

Fig. 8. RAOs at AX5 for different wave directions, showing vertical displacement (top), weak axis bending moment (middle) and strong axis bending moment (bottom)

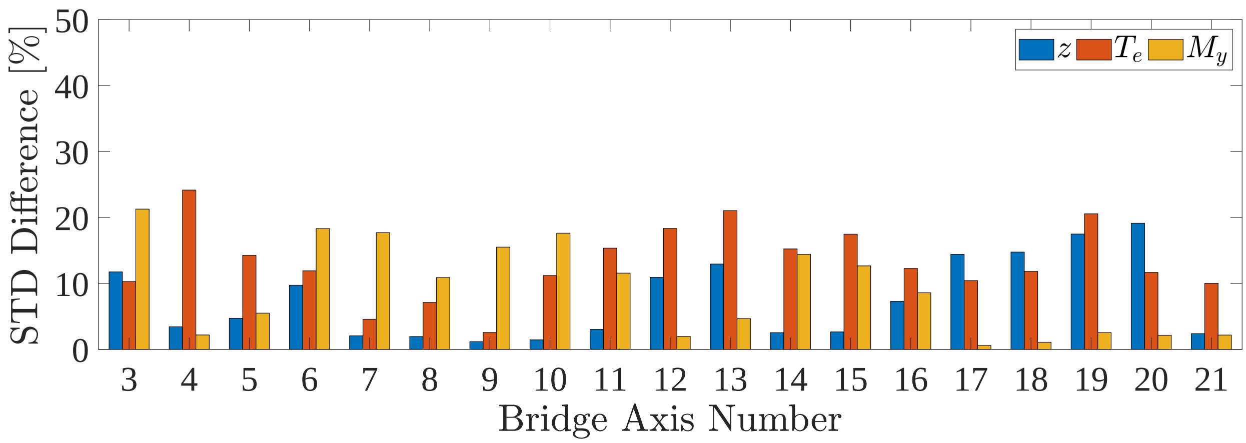

Fig. 9. Average absolute differences in standard deviation of bridge girder response along the bridge for all six simulations of load case LC1.

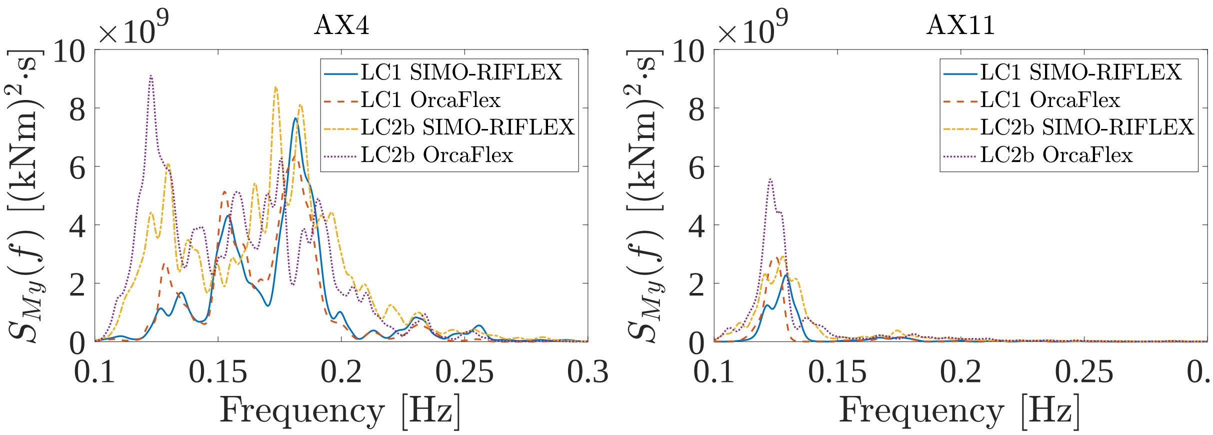

Fig. 10. A comparison of weak axis bending moment response spectra at AX4 and AX11 for load case LC1 and LC2b

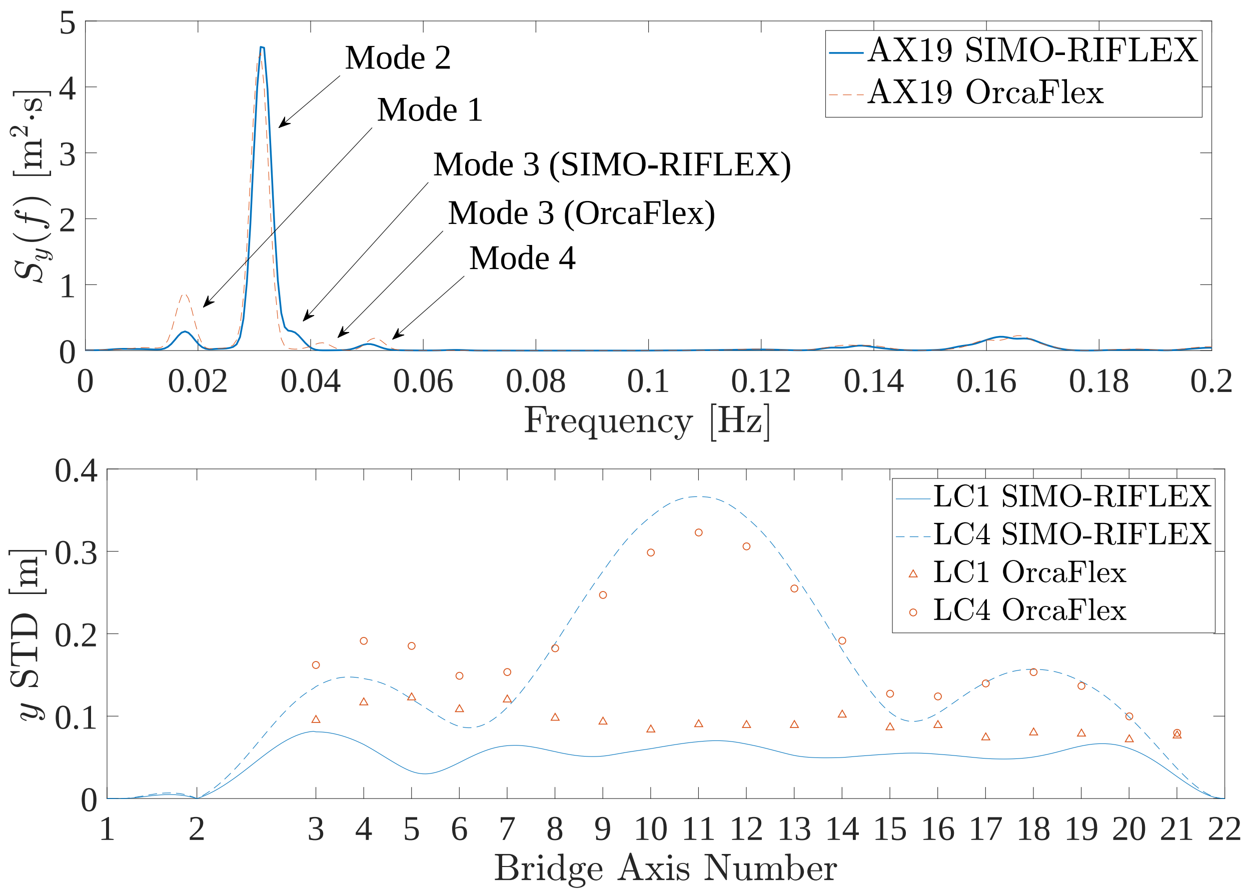

Fig. 11. Effect of including second order wave loads in the analysis. Response spectrum of transverse displacement at AX19 (top) and comparison of standard deviation of transverse displacement along the bridge (bottom).

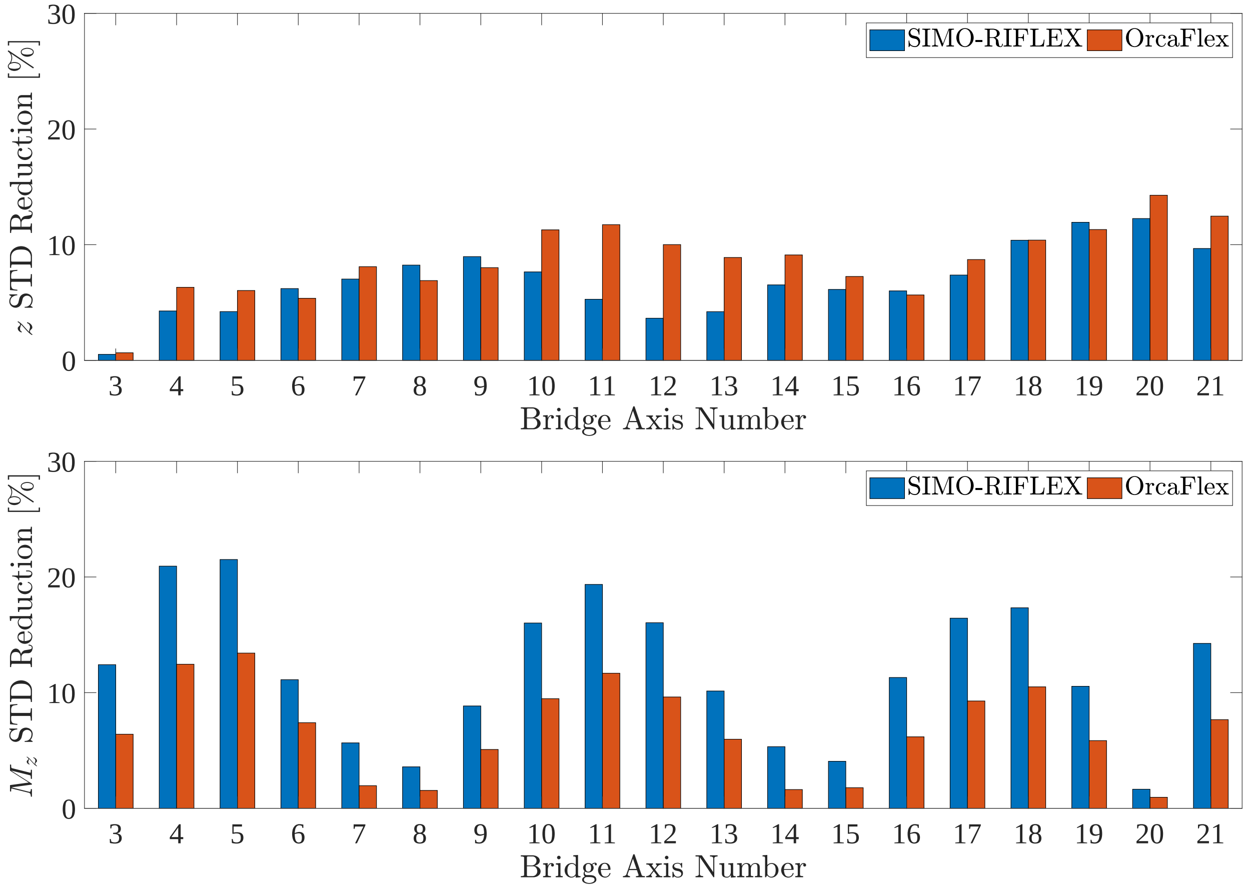

Fig. 12. Reduction in standard deviation of responses when including viscous effects. Reduction in vertical displacement going from load case LC2b to LC3 (top) and reduction in strong axis bending moment going from load case LC4 to LC5 (bottom).

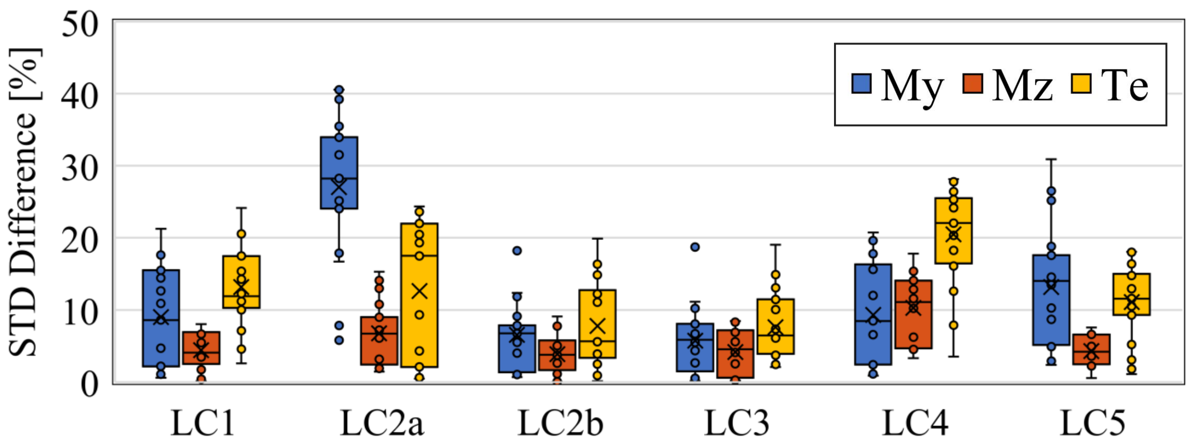

Fig. 13. Box plots of the absolute difference in the standard deviation of the response for load effects in the different load cases. LC2a and LC2b are with SIMO-RIFLEX default and manually specified angles in the spreading function, respectively. The × indicate the average value along the bridge axes.